Dust Properties of C II Detected z ~ 5.5 Galaxies: New HST/WFC3 Near-IR Observations

Barisic, I.; Faisst, A. L.; Capak, P. L.; Pavesi, R.; Riechers, D. A.; Scoville, N. Z.; Cooke, K.; Kartaltepe, J. S.; Casey, C. M.; Smolčić, Vernesa

Repository / Repozitorij:

Repository of the Faculty of Science - University of Zagreb

Dust Properties of C II Detected $z \sim 5.5$ Galaxies: New *HST*/WFC3 Near-IR Observations

I. Barisic[1,2] , A. L. Faisst[3] , P. L. Capak[3], R. Pavesi[4] , D. A. Riechers[4] , N. Z. Scoville[5] , K. Cooke[6] , J. S. Kartaltepe[6], C. M. Casey[7] , and V. Smolcic[1]

[1] Department of Physics, Faculty of Science, University of Zagreb, Bijenička cesta 32, 10000 Zagreb, Croatia; barisic@mpia.de
[2] Max-Planck Institut für Astronomie, Königstuhl 17, D-69117, Heidelberg, Germany
[3] Infrared Processing and Analysis Center, California Institute of Technology, Pasadena, CA 91125, USA
[4] Department of Astronomy, Cornell University, Space Sciences Building, Ithaca, NY 14853, USA
[5] Cahill Center for Astronomy and Astrophysics, California Institute of Technology, Pasadena, CA 91125, USA
[6] School of Physics and Astronomy, Rochester Institute of Technology, 84 Lomb Memorial Drive, Rochester, NY 14623, USA
[7] Department of Astronomy, The University of Texas at Austin, 2515 Speedway Boulevard, Stop C1400, Austin, TX 78712, USA
Received 2017 March 17; revised 2017 May 19; accepted 2017 July 6; published 2017 August 9

Abstract

We examine the rest-frame ultraviolet (UV) properties of 10 [C II]$\lambda158\,\mu$m-detected galaxies at $z \sim 5.5$ in COSMOS using new *Hubble Space Telescope*/Wide Field Camera 3 near-infrared imaging. Together with pre-existing 158 μm continuum and [C II] line measurements by the Atacama Large Millimeter/submillimeter Array, we study their dust attenuation properties on the IRX–β diagram, which connects the total dust emission ($\propto$ IRX $= \log(L_{FIR}/L_{1600})$) to the line-of-sight dust column ($\propto \beta$). We find systematically bluer UV continuum spectral slopes (β) compared to previous low-resolution ground-based measurements, which relieves some of the tension between models of dust attenuation and observations at high redshifts. While most of the galaxies are consistent with local starburst or Small Magellanic Cloud–like dust properties, we find galaxies with low IRX values and a large range in β that cannot be explained by models of a uniform dust distribution well mixed with stars. A stacking analysis of Keck/DEIMOS optical spectra indicates that these galaxies are metal-poor with young stellar populations that could significantly alter their spatial dust distribution.

Key words: dust, extinction – galaxies: evolution – galaxies: formation – galaxies: high-redshift – galaxies: ISM

1. Introduction

Galaxies at $z > 4$ likely have different interstellar medium (ISM) properties than galaxies in the local universe (e.g., Carilli & Walter 2013). For example, studies of emission line ratios of high-redshift ($z > 4$) galaxies by *Spitzer* suggest that early galaxies grow at a fast pace, with high specific star formation rates (SFRs) and stellar mass assembly timescales of only a couple of hundred Myr (de Barros et al. 2014; Faisst et al. 2016a; Jiang et al. 2016). A substantially higher gas fraction as well as changes in the ionization parameter of stellar radiation indicated by the [O III]/[O II] line ratio are also observed, indicative of a different H_2 region configuration (Steidel et al. 2014; Genzel et al. 2015; Silverman et al. 2015; Faisst 2016; Masters et al. 2016; Scoville et al. 2016).

So far, direct studies of the ISM at $z > 4$ have been difficult due to the lack of sensitivity in the far-infrared (FIR) and submillimeter (submm) wavelengths where the key ISM diagnostics are present. With the Atacama Large Millimeter/submillimeter Array (ALMA) it is now possible to study the ISM of galaxies at very high redshifts via the measurement of the [C II] 158 μm emission and the FIR continuum. Some of the first studies of $z > 4$ galaxies with ALMA find significantly lower dust continuum emission than those found in local galaxies (Riechers et al. 2014; Capak et al. 2015; Maiolino et al. 2015; Schaerer et al. 2015; Watson et al. 2015; Carilli et al. 2016; Dunlop 2016; Knudsen et al. 2016).

Studying a sample of 10 Lyman break galaxies (LBGs) at $5 < z < 6$, Capak et al. (2015, hereafter C15) find the ratio of infrared to ultraviolet light (L_{FIR}/L_{1600} = IRX) at a given UV continuum spectral slope (β) in the so-called IRX–β relation to be significantly lower than what was expected from dust

attenuation models (e.g., Charlot & Fall 2000) or even in local low-metallicity galaxies like the Small Magellanic Cloud (SMC; Pettini et al. 1998). Furthermore, there are galaxies with exceptionally red β slopes at low IRX values, which are difficult to physically explain (Charlot & Fall 2000). These findings are curious and, if confirmed, would imply a substantial evolution of ISM properties in the first 1 billion years of the universe. These measurements leave significant uncertainty in what is physically occurring. First, the FIR luminosities are derived from a single ALMA continuum point at rest-frame 158 μm, which means significant assumptions on the shape of the FIR spectral energy distribution (SED) must be made. Second, the β measurements are derived from low signal-to-noise ratio (S/N) ground-based data, which results in significant systematic uncertainty (e.g., Dunlop et al. 2012; Rogers et al. 2013).

In this paper, we present deep *Hubble Space Telescope* (*HST*) near-IR imaging to provide improved measurements of β and the UV luminosity (L_{1600}) for the 10 originally targeted galaxies, 2 serendipitous sources, and 2 subcomponents of 1 of the galaxies that are resolved by *HST* at $z \sim 5.5$ presented in C15 (Section 2). We carefully investigate potential systematics in the derivation of these parameters by performing extensive simulations to eventually pinpoint the location of these galaxies on the IRX–β plane (Sections 3 and 4). A companion paper (A. L. Faisst et al. 2017, in preparation) presents an additional analysis of the dust temperatures and far-infrared properties of these galaxies given a sample of local galaxies.

We assume a flat cosmology with $\Omega_{\Lambda,0} = 0.7$, $\Omega_{m,0} = 0.3$, and $h = 0.7$. Magnitudes are quoted in AB (Oke 1974).
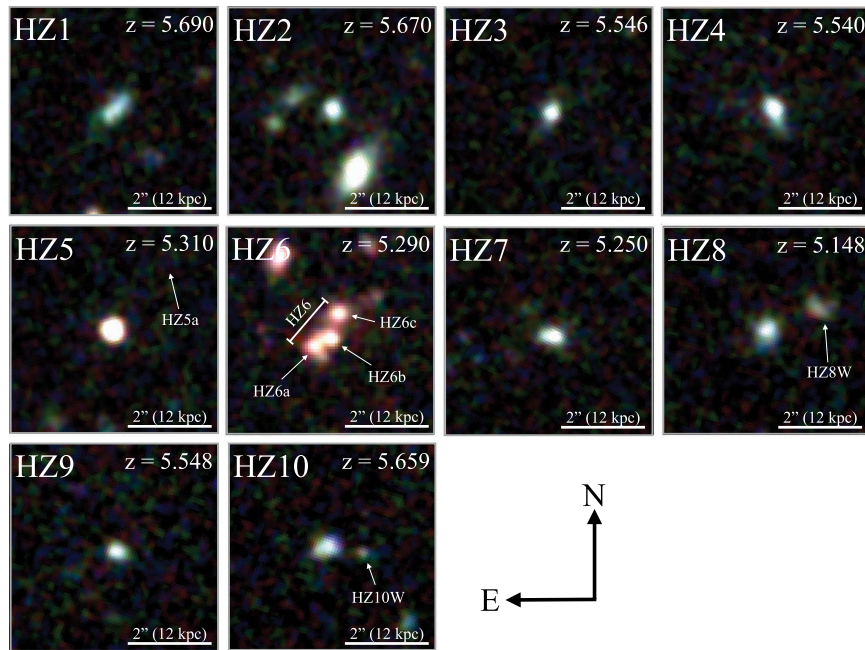
Figure 1. *HST*/WFC3 color (F105W, blue; F125W, green; F160W, red) cutouts from the 10 pointings. The two serendipitous [C II] detections HZ5a and HZ8W and other subcomponents are indicated by white arrows.

2. Data

2.1. Sample Selection and Auxiliary Data

The sample that is used in this work is based on C15, and we summarize its properties in the following paragraphs. The sample consists of nine star-forming LBGs at one to four times the characteristic luminosity (L^*) and one low-luminosity quasar (HZ5) observed at $5 < z < 6$ in the 2 square-degree field of the *Cosmic Evolution Survey* (*COSMOS*; Scoville et al. 2007),[8] which provides a multitude of photometric data (Laigle et al. 2016). The 10 galaxies are initially selected by a range of techniques and designed to be complete in quantities and are followed up with the *Deep Extragalactic Imaging Multi-Object Spectrograph* (*DEIMOS*; Faber et al. 2003) to confirm their redshifts spectroscopically via the rest-frame UV absorption features. Out of 10 galaxies, 6 show a strong Lyα emission, while 3 show only weak emission. No Lyα was detected in HZ3. The galaxies cover a large range in SFRs and stellar masses (see C15), and the UV absorption features suggest gas-phase metallicities of $12 + \log(O/H) = 8.0$–8.5, representative of the average metallicity of $\log(M/M_\odot) \sim 10$ galaxies at $z \sim 5$ (Faisst et al. 2016b). The galaxies were observed with ALMA[9] targeting the wavelength around rest-frame 158 μm including the FIR continuum and the [C II] emission line (Capak et al. 2015). All galaxies were detected in [C II] and four of them have detected the FIR continuum. In addition, 2 serendipitously detected [C II] emitters (HZ5a and HZ8W) were found at the same [C II] redshift of HZ5 and HZ8 at a projected distance of 10–15 kpc, and *HZ6* breaks into 3 subcomponents for a total of 14 objects (Figure 1).

2.2. New HST/WFC3 Observations

To study the rest-frame UV properties of these galaxies, we have obtained *HST*/Wide Field Camera 3 (WFC3) imaging between 2015 March and July (*HST* Cycle 22, ID 13641, PI: P. L. Capak) in F105W, F125W, and F160W corresponding to 1.05 μm, 1.25 μm, and 1.54 μm, respectively. The 10 galaxies were observed in 10 separate pointings for 1 orbit per filter reaching 26.2, 26.4, and 25.9 AB (5σ in $1''$ aperture). Note that HZ6 was observed in another *HST* program (*HST* Cycle 21, ID 13384, PI: D. Riechers) to which we added F105W. The standard *HST* data reduction procedure as explained in the *HST* Data Handbook[10] was used to convert the raw data frames into the final flat-fielded and flux-calibrated science products. Thereby we used the Pyraf/STSDAS `calfw3` task to create a bad pixel array and to perform the bias and dark current subtraction of the readouts. Geometric distortions have been corrected for using the latest distortion solutions (2012 March 22) provided by the STScI/WFC3 web page and the exposures are joined using the Pyraf/STSDAS `AstroDrizzle` task. We use the *HST*/ACS F814W images available on the COSMOS field for the astrometric alignment of the frames to reach subarcsecond precision (K. Cooke et al. 2017, in preparation). Figure 1 shows *HST*/WFC3 three-color cutouts of each of the 10 pointings.

3. Measurements and Simulations

The UV continuum slope β for star-forming galaxies at high-z is dominated by the line-of-sight dust column density, which attenuates the UV light of the star-forming regions.[11] It is therefore a valid tool to study the ISM column density of

---

[8] http://cosmos.astro.caltech.edu
[9] ALMA Cycle 1, ID 13641, PI: P. L. Capak. See C15 for a detailed description of this data.

[10] http://www.stsci.edu/hst/wfc3/analysis
[11] Note that β also depends on internal properties of a galaxy such as the age and metallicity of a stellar population as well as its star formation history. However, these have less effect on the overall β at high redshifts as compared to dust (see Figure 13 in Bouwens et al. 2012)
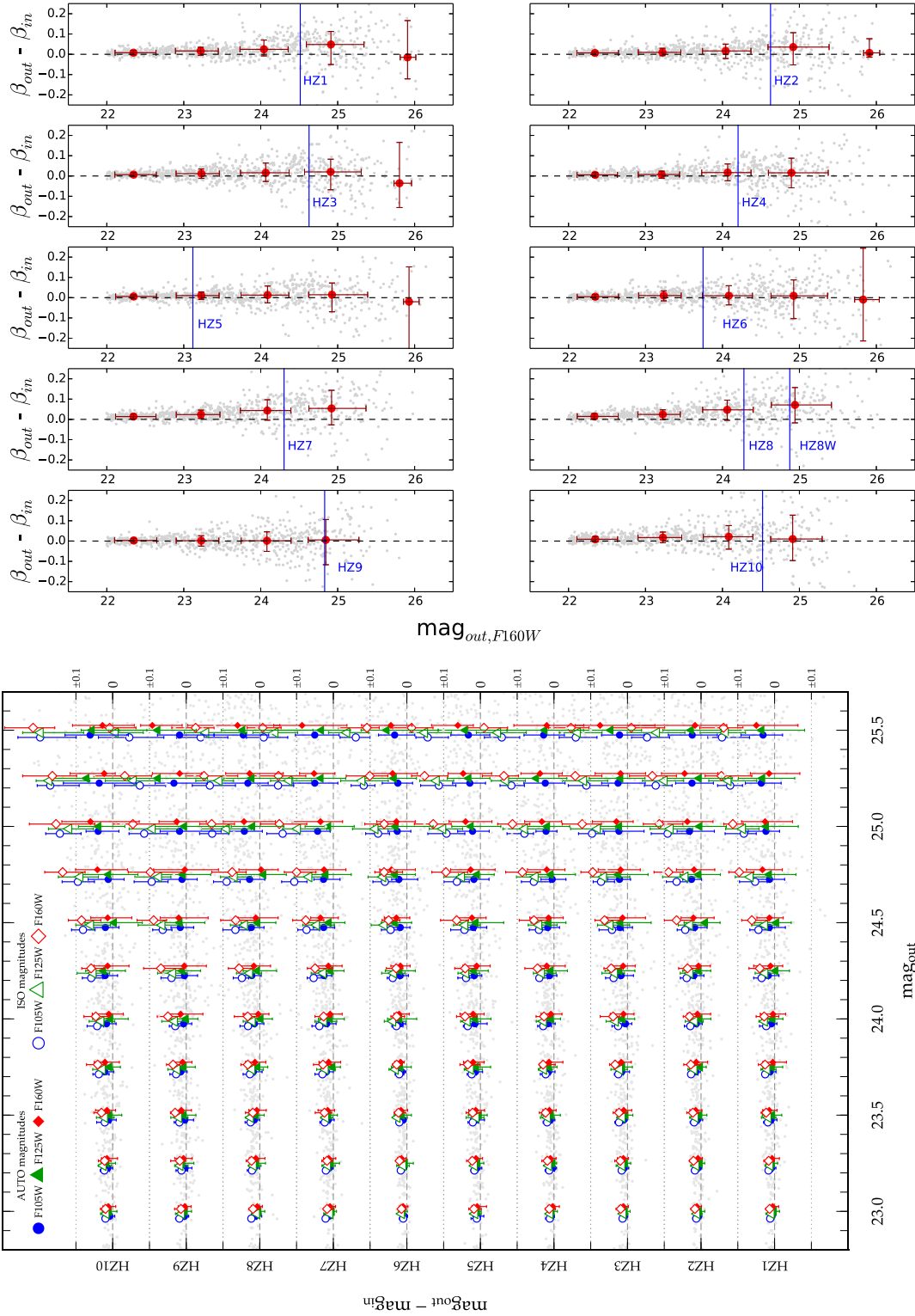
Figure 2. Results from our simulations. Top: recovering error of β as a function of output F160W magnitude for each *HST* pointing (gray for single galaxies; red in bins of magnitude). The simulation suggests no significant biases. Bottom: recovering error in F105W (blue dots), F125W (green triangles), and F160W (red diamonds) magnitudes for the 10 *HST* pointings (filled: AUTO magnitude; open: *ISO* magnitudes). *ISO* magnitudes deviate systematically from the true by more than 0.1 mag at >24.5 AB in comparison to AUTO magnitudes (<0.1 mag up to 25.5 AB).

galaxies (Meurer et al. 1999; Kong et al. 2004; Casey et al. 2014). Furthermore, β is the only estimate of the dust content available for the vast majority of galaxies at $z > 3$ due to the relative insensitivity of contemporary optical and IR surveys. The β can be combined with IRX, which is sensitive to the total

amount of dust, to form the IRX–β relation which can be used to infer the evolution of ISM properties.

The measurement of β at high redshifts is not trivial due to the scarcity of photometric bands covering the rest-frame UV part of the galaxies' SEDs and low sensitivity from the ground.

Table 1
Summary of *HST* Ultraviolet and ALMA FIR Measurements for the C15 Sample

| ID | Redshift | *HST* Based Measurements (This Work) | | | | | ALMA FIR Measurements[a] | |
		F105W	F125W	F160W	β	$\log(L_{1600}/L_\odot)$	$\log(L_{\rm FIR}/L_\odot)$	$\log(L_{\rm C\,II}/L_\odot)$
HZ1	5.690	24.53 ± 0.04	24.31 ± 0.03	24.52 ± 0.05	$-1.88^{+0.12}_{-0.10}$	11.21 ± 0.01	<10.32	8.40 ± 0.32
HZ2	5.670	24.65 ± 0.03	24.50 ± 0.03	24.63 ± 0.05	$-1.82^{+0.11}_{-0.11}$	11.15 ± 0.01	<10.30	8.56 ± 0.41
HZ3	5.546	24.74 ± 0.04	24.57 ± 0.03	24.63 ± 0.04	$-1.71^{+0.09}_{-0.08}$	11.08 ± 0.01	<10.53	8.67 ± 0.28
HZ4	5.540	24.17 ± 0.02	24.21 ± 0.02	24.20 ± 0.03	$-2.05^{+0.11}_{-0.10}$	11.28 ± 0.01	11.13 ± 0.54	8.98 ± 0.22
HZ5	5.310	23.48 ± 0.01	23.53 ± 0.01	23.12 ± 0.01	$-1.03^{+0.03}_{-0.02}$	11.45 ± 0.01	<10.30	<7.20
HZ5a	5.310	>26.24[b]	>26.35[b]	>25.89[b]	…	<10.37[b]	<10.30	8.15 ± 0.27
HZ6 (total)[c]	5.290	23.62 ± 0.03	23.45 ± 0.04	23.29 ± 0.03	$-1.15^{+0.19}_{-0.21}$	11.47 ± 0.10	11.13 ± 0.23[c]	9.23 ± 0.04[c]
· HZ6a[d]	…	25.28 ± 0.36	24.90 ± 0.30	24.67 ± 0.25	$-0.54^{+0.47}_{-0.72}$	11.11 ± 0.07	10.26 ± 0.23[d]	8.32 ± 0.06[d,e]
· HZ6b[d]	…	24.77 ± 0.28	24.65 ± 0.33	24.58 ± 0.37	$-1.51^{+0.62}_{-0.72}$	11.00 ± 0.07	10.87 ± 0.23[d]	8.81 ± 0.02[d,e]
· HZ6c[d]	…	24.53 ± 0.16	24.43 ± 0.13	24.25 ± 0.10	$-1.30^{+0.72}_{-0.60}$	10.81 ± 0.07	10.79 ± 0.23[d]	8.65 ± 0.03[d]
HZ7	5.250	24.56 ± 0.04	24.42 ± 0.03	24.30 ± 0.03	$-1.38^{+0.15}_{-0.09}$	11.05 ± 0.02	<10.35	8.74 ± 0.24
HZ8	5.148	24.51 ± 0.04	24.37 ± 0.04	24.28 ± 0.04	$-1.41^{+0.13}_{-0.12}$	11.04 ± 0.02	<10.26	8.41 ± 0.18
HZ8W	5.148	25.68 ± 0.11	25.14 ± 0.07	24.88 ± 0.08	$-0.17^{+0.32}_{-0.25}$	10.57 ± 0.04	<10.26	8.31 ± 0.23
HZ9	5.548	24.99 ± 0.06	24.91 ± 0.05	24.83 ± 0.07	$-1.59^{+0.27}_{-0.20}$	10.95 ± 0.02	11.54 ± 0.19	9.21 ± 0.09
HZ10	5.659	24.56 ± 0.05	24.48 ± 0.05	24.52 ± 0.06	$-1.88^{+0.17}_{-0.12}$	11.14 ± 0.02	11.94 ± 0.08	(9.60 ± 0.13)[f]
· HZ10W[g]	…	26.83 ± 0.16	26.86 ± 0.13	26.63 ± 0.15	$-1.61^{+0.49}_{-0.47}$	10.23 ± 0.05	(11.64 ± 0.08)[g]	(8.93 ± 0.13)[g]

Notes.
[a] Measurements by C15 unless noted differently. The FIR luminosity is integrated between 3 μm and 1100 μm.
[b] 5 σ limits in 1″ aperture.
[c] Integrated photometry of all the subcomponents. The ALMA measurements are from Pavesi et al. (2016).
[d] The photometry for the subcomponents of HZ6 is measured by GALFIT. The ALMA properties are re-extracted using the F160W data as a spatial prior.
[e] The quoted uncertainties are formal fitting uncertainties. The actual uncertainties for HZ6a and HZ6b are larger (up to 0.2 dex) due to severe blending.
[f] Updated value from Pavesi et al. (2016).
[g] Photometry measured in a 0″5 aperture. We assume half the FIR and [C II] luminosity of HZ10.

Furthermore, the measurement of β is particularly sensitive to the signal to noise of photometry and systematics in flux measurements, such as confusion from neighboring sources, background subtraction, and surface brightness effects (e.g., Dunlop et al. 2012; Finkelstein et al. 2012; Rogers et al. 2013; Bouwens et al. 2014). High S/N data accompanied by simulations are therefore essential for correcting for these effects. In the following sections, we describe the measurement of the β and the methods used to access and correct systematic uncertainties.

3.1. Flux Extraction and Measurement of β

We use *Source Extractor* (version 2.5.0; Bertin & Arnouts 1996) to measure the fluxes of the 14 galaxies in F105W, F125W, and F160W. For each of the galaxies, we manually tune the *Source Extractor*'s input parameters in order to optimize the de-blending, object detection, and background subtraction. The fluxes are measured in different aperture types including *ISO*, AUTO, as well as three manual apertures with radii $r = 0″8, 0″9$, and $1″0$. The isophotal flux threshold was set to 2σ relative to the weight map and the AUTO apertures use a minimum radius of 3.5 pixels ($0″45$) for low S/N sources. From the comparison of the input versus output magnitudes from our simulations (described in Section 3.2) as well as from a visual inspection of the output photometry, we find that the AUTO aperture magnitudes have the least systematic biases (Figure 2).

In addition to the 12 main measurements, the photometries of the subcomponents of HZ6 are extracted using GALFIT (version 3.0.5; Peng et al. 2010) and additionally verified by manual apertures (agreement to better than 0.1 mag).

The FIR [C II] line emission and 158 μm continuum fluxes at the positions of the three subcomponents are fitted by Gaussians with the size of the ALMA beam ($\sim 0″5$). HZa and HZb are significantly blended with ALMA, and therefore the relative flux extraction is uncertain by up to a factor of three depending on the weighting.

The UV spectral slopes of the galaxies are measured directly from the F105W, F125W, and F160W photometric bands, which correspond to rest-frame 1600–2400 Å at $z \sim 5.5$. We note that the effective center wavelength of the filters changes with the power-law function $f_\lambda \propto \lambda^\beta$ and must be accounted for in the measurement of β, as the filter transmission curves have a finite width and a calibration on the AB system assumes $\beta = -2$. We therefore use a forward-modeling approach to measure β for our galaxies. From a tightly spaced grid in intrinsic spectral slopes ($\beta_{\rm in}$) and intercepts (C), we create power-law SEDs according to $\log(f_\lambda) = \beta_{\rm in} \times \log(\lambda) + C$, which we convolve with the three filter transmission curves for F105W, F125W, and F160W, respectively. The best $\beta_{\rm in}$ is then found via χ_2—minimization from the comparison of the previously obtained model fluxes and the measured fluxes of the galaxies. We obtain estimates of the measurement uncertainties on β by repeating the above steps and thereby varying the observed fluxes within their errors (assuming a Gaussian error distribution). The extracted photometry of the galaxies as well as the final β and L_{1600} with 1σ uncertainties are listed in Table 1.

3.2. Simulations

We now assess possible systematic uncertainties of our β measurements arising from biases in the extraction of the photometry. For this, we create model galaxies, which are
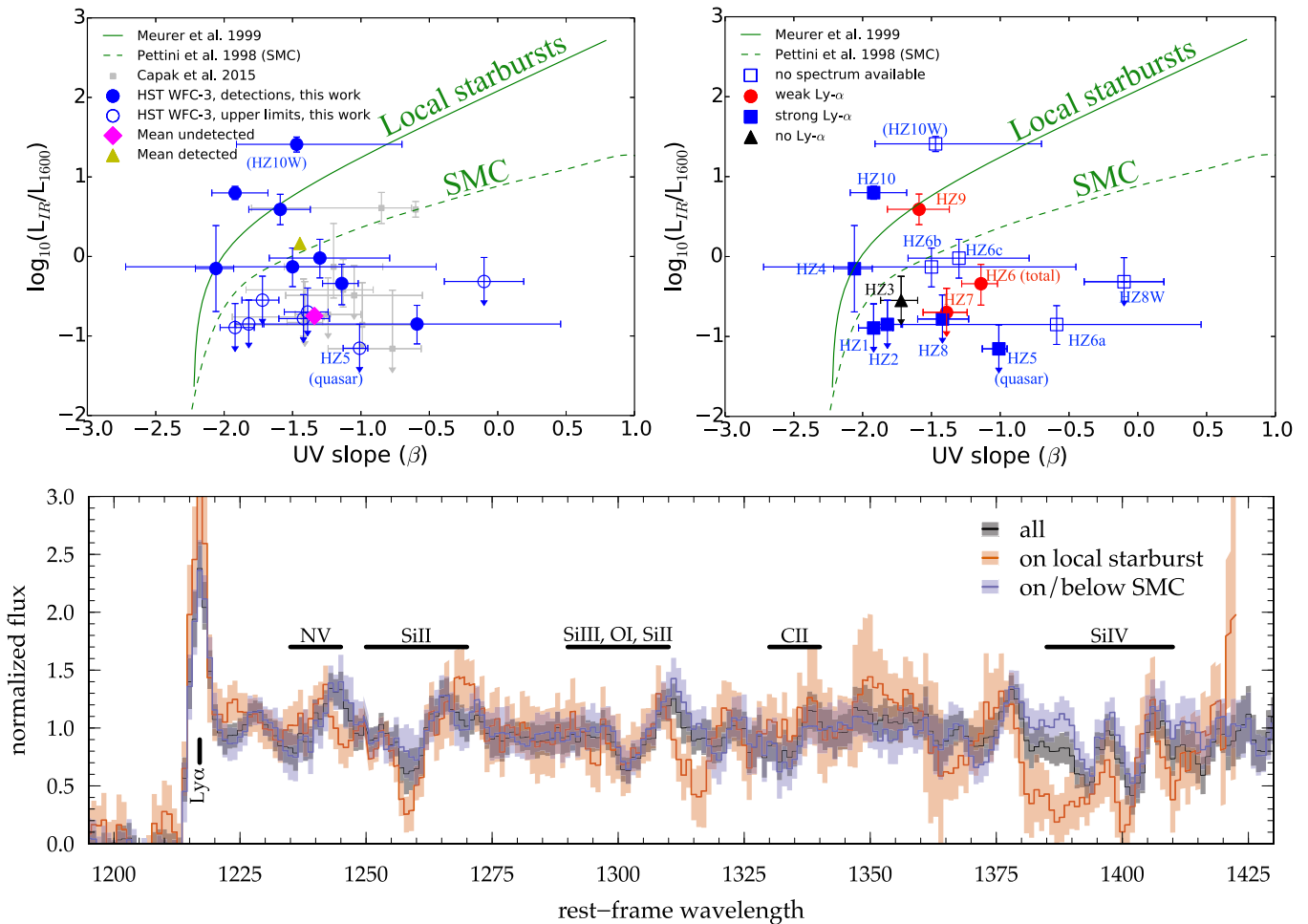
Figure 3. IRX–β diagram and spectral properties of our $z \sim 5.5$ galaxies. Upper left: the blue symbols show updated β and L_{1600} measurements, and the mean values of detected (undetected) sources are shown with a yellow (magenta) symbol. The previous measurements from C15 are shown by gray symbols. We also show relations from the literature, as indicated in the legend. Upper right: galaxies color-coded according to their Lyα strength. We do not see a relation between Lyα emission and position on the IRX–β diagram. Bottom: stacked Keck/DEIMOS spectra for galaxies falling on the local starburst relation (HZ4, HZ9, and HZ10; red) and below the SMC relation (blue). The black line shows all nine galaxies (excluding the low-luminosity quasar HZ5). The 1σ uncertainties are indicated in colored bands.

placed onto the original *HST* pointings and re-extracted with the same parameters used for the real galaxies. Following our approach in Section 3.1, we create 1000 random model SEDs with $-3 < \beta < 2$ and $22 < \text{mag}_{F160W} < 26$, from which we obtain F105W, F125W, and F160W total fluxes by convolving with the respective filter transmission curves. The actual model galaxies are parameterized by a two-dimensional Gaussian light distribution scaled to their total fluxes in each filter and with half-light sizes equal to the median measured for the real galaxies in the respective filters ($\sim 0\rlap{.}''17$). The model galaxies are then placed randomly in empty spots on each of the 10 *HST* calibrated pointings. For this we stack the segmentation images in all three filters as returned by *Source Extractor* and require a box of 20×20 pixels of clean sky background around the coordinate at which the model galaxies is inserted onto the frame. The model galaxies are re-extracted and analyzed in the same way as the real galaxies in order to obtain their output fluxes and spectral slope (β_{out}).

Figure 2 shows the results of our simulations. Each of the 10 panels in the top figure corresponds to one *HST* pointing and shows the difference $\beta_{out} - \beta_{in}$ as a function of output F160W magnitude. The observed magnitude of the 10 galaxies in each frame including the 2 serendipitous [C II] detections is

indicated with blue lines. The increase in scatter for fainter magnitudes (i.e., lower S/N) is clearly visible. For brighter magnitudes we find a fast convergence to $\beta_{out} - \beta_{in} = 0$ as expected. In general, we find systematic offsets in our β measurements of less than $\Delta\beta = 0.05$ at the observed magnitudes of our galaxies, which is several factors less than the actual measurement uncertainties. We therefore conclude that our β measurements are robust and not significantly biased. We also note that the scatter from the true β seen in the simulation is consistent with the 1σ uncertainty we derive for the β measurements (see Table 1), which suggests that the dominant factor of uncertainty is photometric and a power-law approximation for the galaxies' SEDs is reasonable. We do not find significant biases (<0.05 mag up to 25.5 AB) in recovering the AUTO magnitudes (lower panel in Figure 2). We note that *ISO* magnitudes are systematically biased at >24.5 AB by 0.1 mag due to surface brightness effects, and we therefore prefer to use AUTO magnitudes instead.

4. Results and Discussion

The upper left panel of Figure 3 shows the updated location of the galaxies in blue. The UV luminosities of our study

and C15 are in good agreement within the errors. Our new *HST* based β measurements are consistent within errors with C15, but we find a systematic bias of the previous ground-based data toward redder slopes. This is due to the low S/N and systematic uncertainties of that data as noted by C15 that add a 0.3 dex systematic error bar on their measurements. Importantly, we have pinned down the β of the $z \sim 5.5$ galaxies with our new observations with sufficient precision and accuracy to make quantitative statements about the evolution of the IRX–β relation. We find that roughly two-thirds of the galaxies are consistent with the dust attenuation models of local starbursts or the SMC. However, one-third consists of low IRX objects residing *below* the SMC curve with a large range in β. Interestingly, some of them are very red, suggesting a significant dust attenuation along the line of sight, while their low IRX values indicate only very little radiation in the IR, i.e., an overall low dust mass. This is at odds with SMC dust properties, as well as other theoretical models that assume dust in thermal equilibrium at ~ 30 K that is well mixed with stars (e.g., Charlot & Fall 2000). To explain these observations, either the physical properties of the dust or the geometry of its spatial distribution have to change. In an upcoming paper, we will investigate this further by investigating in detail the dust temperature and its spatial distribution in high-redshift galaxies (A. L. Faisst et al. 2017, in preparation).

The $R = 3000$–4500 Keck/DEIMOS optical spectra that are available for all nine main galaxies[12] allow us to investigate further the spectroscopical properties of the galaxies across the IRX–β diagram. The upper right panel of Figure 3 shows the IRX–β diagram with galaxies grouped in strong, weak, and no Lyα emitters. We do not see a trend with Lyα emission strength. The lower panel of Figure 3 shows median stacks of the spectra of galaxies with dust properties similar to the local starbursts (HZ4, HZ9, and HZ10) and galaxies below the SMC dust attenuation curve. The spectra are binned to 1 Å, and the 1σ uncertainties are derived by repeating the stacking analysis 500 times including Gaussian measurement uncertainties. This indicates that galaxies similar to local starbursts show deeper absorption in the Si II and Si IV doublet ISM lines at 1260 Å and 1400 Å, respectively, compared to galaxies below the SMC dust relation. Furthermore, there is indication of a flux deficit around N V (~ 1240 Å) and an upturn at 1225 Å. Such UV absorption features correlate well with the dust column density and gas-phase metallicity of galaxies (e.g., Heckman et al. 1998; Leitherer et al. 2011; Faisst et al. 2016b). Our findings therefore emphasize the diversity of galaxies at $z \sim 5.5$. Galaxies close to the local starburst relation are likely more evolved and metal-rich, while galaxies below the SMC relation that show weaker UV absorption features are dust-poor and metal-poor and possibly of a younger age (see also Reddy et al. 2010). Importantly, these young galaxies can have substantially altered spatial dust distributions, which lead to the variety of UV spectral slopes at low IRX values. Specifically, clouds of dust may be expelled into the circumgalactic regions of these galaxies by interactions with their environment or internal radiation pressure and turbulences due to vigorous star formation. The serendipitous detections around HZ8 and the quasar HZ5 suggest a significant amount of circumgalactic material out to at least the 10 kpc projected radius. HZ5 has only a narrow Lyα emission (30 Å equivalent width and 10 Å

FWHM; Mallery et al. 2012), and its UV absorption features are at the same redshift as those indicated by the [C II] emission of HZ5a. This is indicative of the UV undetected HZ5a absorbing a substantial part of the quasar's light. HZ8W shows one of the reddest β but lowest IRX values that could hint toward a several kiloparsec extended foreground dust screen of HZ8. HZ10W and the components of HZ6 might be representative of a similar situation. Future follow-up observations of these objects with the *James Webb Space Telescope* will be important to further study the intergalactic medium around these galaxies.

5. Conclusion

We have obtained deep *HST* near-IR imaging to accurately measure the UV spectral slopes and luminosities of 14 $z \sim 5.5$ galaxies in total. We combine these new measurements with previous ALMA observations at 158 μm available for all of these galaxies to investigate the IRX–β diagram at $z \sim 5.5$. The main findings and results of this paper are as follows:

1. Our new *HST* observations greatly reduce the uncertainties and biases in UV spectral slopes compared to previous ground-based measurements. Most of the galaxies at $z \sim 5.5$ are either consistent with local starbursts or dust properties similar to the SMC.
2. The galaxies occupy a large range in IRX–β parameter space, indicative of a large diversity in their properties even 1 billion years after the Big Bang.
3. We find galaxies with low IRX values and large ranges of β, which cannot be explained by SMC-like dust or models of well-mixed stars and dust in thermal equilibrium. Instead, the fundamental dust properties or the geometry of dust distribution have to change.
4. Stacked rest-UV spectra of the galaxies across the IRX–β diagram are indicative of a range of metallicities and evolutionary stages of the galaxies. In particular, galaxies close to or below the SMC relation show weak UV absorption features indicative of low dust and metal content.

---

[12] We do not consider the low-luminosity quasar HZ5 here.

ORCID iDs

I. Barisic ⓘ https://orcid.org/0000-0001-6371-6274
A. L. Faisst ⓘ https://orcid.org/0000-0002-9382-9832
R. Pavesi ⓘ https://orcid.org/0000-0002-2263-646X
D. A. Riechers ⓘ https://orcid.org/0000-0001-9585-1462
N. Z. Scoville ⓘ https://orcid.org/0000-0002-0438-3323
K. Cooke ⓘ https://orcid.org/0000-0002-2200-9845
C. M. Casey ⓘ https://orcid.org/0000-0002-0930-6466

References

Bertin, E., & Arnouts, S. 1996, A&AS, 117, 393
Bouwens, R. J., Illingworth, G. D., Oesch, P. A., et al. 2012, ApJ, 754, 83
Bouwens, R. J., Illingworth, G. D., Oesch, P. A., et al. 2014, ApJ, 793, 115
Capak, P. L., Carilli, C., Jones, G., et al. 2015, Natur, 522, 455
Carilli, C. L., Chluba, J., Decarli, R., et al. 2016, ApJ, 833, 73
Carilli, C. L., & Walter, F. 2013, ARA&A, 51, 105
Casey, C. M., Scoville, N. Z., Sanders, D. B., et al. 2014, ApJ, 796, 95
Charlot, S., & Fall, S. M. 2000, ApJ, 539, 718
de Barros, S., Schaerer, D., & Stark, D. P. 2014, A&A, 563, A81
Dunlop, J. S. 2016, Msngr, 166, 48
Dunlop, J. S., McLure, R. J., Robertson, B. E., et al. 2012, MNRAS, 420, 901
Faber, S. M., Phillips, A. C., Kibrick, R. I., et al. 2003, Proc. SPIE, 4841, 1657
Faisst, A. L. 2016, ApJ, 829, 99
Faisst, A. L., Capak, P., Hsieh, B. C., et al. 2016a, ApJ, 821, 122
Faisst, A. L., Capak, P. L., Davidzon, I., et al. 2016b, ApJ, 822, 29
Finkelstein, S. L., Papovich, C., Salmon, B., et al. 2012, ApJ, 756, 164
Genzel, R., Tacconi, L. J., Lutz, D., et al. 2015, ApJ, 800, 20
Heckman, T. M., Robert, C., Leitherer, C., Garnett, D. R., & van der Rydt, F. 1998, ApJ, 503, 646
Jiang, L., Finlator, K., Cohen, S. H., et al. 2016, ApJ, 816, 16
Knudsen, K. K., Richard, J., Kneib, J.-P., et al. 2016, MNRAS, 462, L6
Kong, X., Charlot, S., Brinchmann, J., & Fall, S. M. 2004, MNRAS, 349, 769
Laigle, C., McCracken, H. J., Ilbert, O., et al. 2016, ApJS, 224, 24
Leitherer, C., Tremonti, C. A., Heckman, T. M., & Calzetti, D. 2011, AJ, 141, 37
Maiolino, R., Carniani, S., Fontana, A., et al. 2015, MNRAS, 452, 54
Mallery, R. P., Mobasher, B., Capak, P., et al. 2012, ApJ, 760, 128
Masters, D., Faisst, A., & Capak, P. 2016, ApJ, 828, 18
Meurer, G. R., Heckman, T. M., & Calzetti, D. 1999, ApJ, 521, 64
Oke, J. B. 1974, ApJS, 27, 21
Pavesi, R., Riechers, D. A., Capak, P. L., et al. 2016, ApJ, 832, 151
Peng, C. Y., Ho, L. C., Impey, C. D., & Rix, H.-W. 2010, AJ, 139, 2097
Pettini, M., Kellogg, M., Steidel, C. C., et al. 1998, ApJ, 508, 539
Reddy, N. A., Erb, D. K., Pettini, M., Steidel, C. C., & Shapley, A. E. 2010, ApJ, 712, 1070
Riechers, D. A., Carilli, C. L., Capak, P. L., et al. 2014, ApJ, 796, 84
Rogers, A. B., McLure, R. J., & Dunlop, J. S. 2013, MNRAS, 429, 2456
Schaerer, D., Boone, F., Zamojski, M., et al. 2015, A&A, 574, A19
Scoville, N., Aussel, H., Brusa, M., et al. 2007, ApJS, 172, 1
Scoville, N., Sheth, K., Aussel, H., et al. 2016, ApJ, 820, 83
Silverman, J. D., Daddi, E., Rodighiero, G., et al. 2015, ApJL, 812, L23
Steidel, C. C., Rudie, G. C., Strom, A. L., et al. 2014, ApJ, 795, 165
Watson, D., Christensen, L., Knudsen, K. K., et al. 2015, Natur, 519, 327